

## Article

# Electrochemical Sensor for the Evaluation of Doxorubicin from Novel Pharmaceutical Formulations and Serum

Alexandra Pusta <sup>1,2</sup>, Mihaela Tertis <sup>1,\*</sup>, Irina Bura <sup>1</sup>, Diana Bogdan <sup>3</sup>, Maria Suciu <sup>3,4</sup>, Simona Mirel <sup>2</sup> and Cecilia Cristea <sup>1</sup>

<sup>1</sup> Department of Analytical Chemistry, Iuliu Hatieganu University of Medicine and Pharmacy, 4 Louis Pasteur Street, 400349 Cluj-Napoca, Romania; alexandra.pusta@umfcluj.ro (A.P.); ccristea@umfcluj.ro (C.C.)

<sup>2</sup> Department of Medical Devices, Iuliu Hatieganu University of Medicine and Pharmacy, 4 Louis Pasteur Street, 400349 Cluj-Napoca, Romania; smirel@umfcluj.ro

<sup>3</sup> National Institute for Research and Development of Isotopic and Molecular Technologies, 67-103 Donat Street, 400293 Cluj-Napoca, Romania; diana.bogdan@itim-cj.ro (D.B.); sucia.maria@ubbcluj.ro (M.S.)

<sup>4</sup> Electron Microscopy Centre “C. Craciun”, Biology and Geology Faculty, Babes-Bolyai University Cluj-Napoca, 5-7 Clinicilor Street, 400006 Cluj-Napoca, Romania

\* Correspondence: mihaela.tertis@umfcluj.ro

**Abstract:** This study focuses on addressing the challenges associated with doxorubicin (DOX), an anthracycline chemotherapeutic widely used in cancer treatment. Despite its efficacy, DOX is linked to severe side effects that limit its clinical applications. Novel pharmaceutical formulations aim to mitigate these issues, providing better safety profiles. The development of these formulations requires analytical methods that can accurately and quickly quantify DOX. A cost-effective and portable electrochemical sensor for DOX detection was developed utilizing in-house printed carbon electrodes decorated with gold nanoparticles. DOX was detected using differential pulse voltammetry. The sensor demonstrated an accurate quantification of DOX from novel pharmaceutical formulations and serum, presenting a dynamic range of 1 to 500 µg/mL and a low detection limit of 0.3 µg/mL. The method, successfully applied to characterize DOX-loaded nanosomes, offers a valuable alternative in the early stages of formulation development, reducing costs and saving time, while maintaining accuracy.

**Keywords:** doxorubicin; nanosomes; in-house produced electrodes; gold nanoparticles; electrochemical detection



**Citation:** Pusta, A.; Tertis, M.; Bura, I.; Bogdan, D.; Suciu, M.; Mirel, S.; Cristea, C. Electrochemical Sensor for the Evaluation of Doxorubicin from Novel Pharmaceutical Formulations and Serum. *Chemosensors* **2024**, *12*, 69. <https://doi.org/10.3390/chemosensors12040069>

Academic Editors: Pedro Salazar and Cristina Tortolini

Received: 28 February 2024

Revised: 10 April 2024

Accepted: 18 April 2024

Published: 19 April 2024



**Copyright:** © 2024 by the authors. Licensee MDPI, Basel, Switzerland. This article is an open access article distributed under the terms and conditions of the Creative Commons Attribution (CC BY) license (<https://creativecommons.org/licenses/by/4.0/>).

## 1. Introduction

Doxorubicin (DOX) is an anthracycline chemotherapeutic, used alone or in combination, in the treatment of cancers of the breast, bladder, ovary and bone, as well as in the treatment of different forms of leukemia and lymphomas [1,2]. Despite its high efficacy, DOX is associated with numerous side effects that are typical of chemotherapy, such as nausea, vomiting, hair loss and decreased immunity. Additionally, it presents a distinctive adverse effect—cardiotoxicity—which can greatly limit its use in the clinical setting. DOX is associated with both acute and chronic cardiotoxicity, with acute toxicity manifesting in the first days after treatment initiation in approximately 11% of patients [3]. Despite being less frequent, chronic cardiotoxicity is irreversible and can be associated with progression to cardiomyopathy or heart failure [3,4].

Because DOX is indispensable in certain chemotherapy regimens, efforts are being made to reduce or postpone the onset of side effects by developing novel DOX pharmaceutical formulations, such as liposomes [5–10]. Two types of liposomal formulations have already been approved and are available on the market—non-PEGylated (Myocet<sup>®</sup>) or PEGylated (Doxil<sup>®</sup>, Lipodox<sup>®</sup>, Caelyx<sup>®</sup>) liposomes containing DOX [11]. These formulations provide better safety profiles compared to non-liposomal DOX, allowing for extended treatment durations. However, currently available liposomal formulations exhibit no increase

in efficacy compared to DOX alone [11,12], demonstrating the need for ongoing research in the development of novel pharmaceutical formulations such as niosomes [13,14], polymeric nanoparticles [15–19] or gels [20], dendrimers [21–23] and magnetic nanocarriers [24–27]. A simple ScienceDirect search using the terms “doxorubicin” and “formulation” is an eloquent example of the increasing interest in this field in the last 10 years (Figure 1).

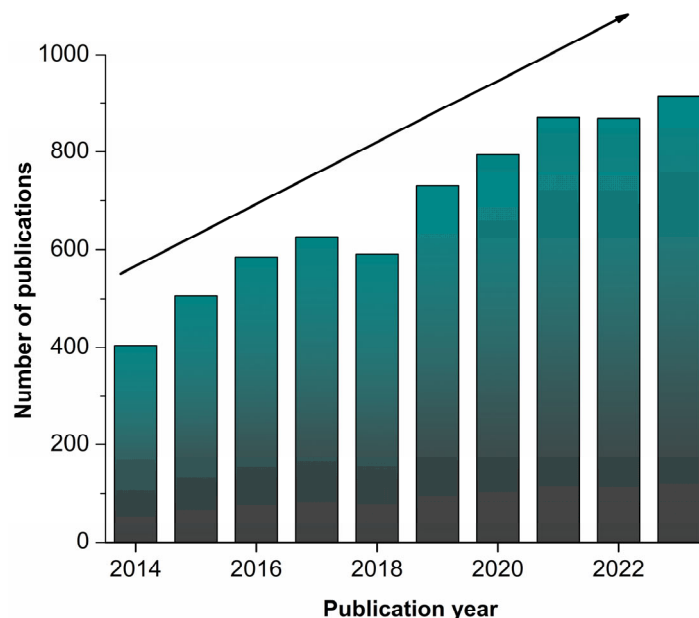


**Figure 1.** The evolution of the number of publications regarding pharmaceutical formulations with DOX in the last 10 years.

In pharmaceutical formulation development, rigorous testing is essential to ensure, among other things, the proper loading and release of drugs from carriers. This is especially important in the optimization stage, where many different parameters are tested and changed to ensure the development of the optimal formulation. In this step, numerous tests need to be carried out to determine the amount of loaded/released substance. In the case of DOX formulations, the most commonly applied quantification methods are spectrophotometric methods [17,18,20,21,25–27] or spectrofluorimetry [19]. Other techniques, such as chromatographic methods [28–33], have also been developed for the quantification of DOX. These methods, while highly accurate, require large volumes of samples, which might not always be available in the early stages of pharmaceutical formulation development. Moreover, they are costly and can require specialized personnel.

Electrochemical methods have emerged as accurate, rapid and portable alternatives to the conventional methods used in drug analysis. The functionalization of electrode surfaces with nanomaterials such as metallic nanoparticles [34,35], carbon nanomaterials [36] or carbide [37] can increase the sensitivity of electrochemical methods for the detection of the target analyte. Direct electrochemical methods relying on platforms modified with carbon-based nanomaterials or metallic nanoparticles have been reported for the detection of DOX from pharmaceutical formulations and biological samples. For example, platinum electrodes were functionalized with multi-walled carbon nanotubes and were used for DOX detection in plasma samples [36]. Silver nanoparticles [35] or silver/gold bimetallic nanoparticles [38] were used to enhance the redox signal of DOX on glassy carbon electrodes, facilitating its detection from plasma, cell lysate [35] and urine [38], respectively. Differential pulse cathodic stripping voltammetry and differential pulse voltammetry were comparatively applied for the detection of DOX on silver solid amalgam electrodes and on a polarized liquid/liquid interface, respectively [39]. Despite the multiple publications on this subject, there is still a considerable need for rapid, accurate, cost-effective and single-use sensors for DOX detection.

In this work, a novel sensor, based on in-house printed electrodes decorated with AuNPs, was proposed for the detection of DOX from pharmaceutical formulations and serum. The electrochemical behavior of DOX on the newly developed electrode surface was extensively analyzed and its detection was performed via differential pulse voltammetry (DPV).

A second objective of this work was the development of DOX-containing nanosomes as proof-of-concept formulations, as well as the application of the developed sensor for the quantification of the DOX loaded and released from the nanosomes. This method was successfully applied for the characterization of these steps, the results obtained being closely correlated to those obtained using UV–Vis spectrophotometry.

The newly developed method offers a cost-effective and portable alternative, without compromising accuracy. While not intended to replace the methods currently used in the pharmaceutical industry, it can be a valuable tool in the initial stages of formulation development, helping to reduce costs and save time when numerous tests are required.

## 2. Materials and Methods

### 2.1. Materials

#### 2.1.1. Chemicals and Reagents

For the electrode fabrication process, carbon conductive ink, Electrodag 423 SS©, was purchased from Henkel (Duseseldorf, Germany) and Ag ink, Electrodag PF-410, was purchased from Acheson (Newark, DE, USA). Doxorubicin hydrochloride (purity  $\geq 95\%$ ) was purchased from Tokyo Chemical Industry Company, Tokyo, Japan. Lipo-N pronanosomes functionalized with surface amino groups were purchased from NanoVex Biotechnologies, Asturias, Spain. All other chemicals used were purchased from Sigma-Aldrich (St. Louis, MO, USA), Fluka Chemie GmbH (Buchs, Switzerland) and Merck (Rahway, NJ, USA). Chemicals and solvents were used as received, without further purification. All solutions were prepared in ultrapure water ( $18 \text{ M}\Omega \text{ cm}^{-1}$ ), which was prepared using a Millipore Simplicity device, Sigma Aldrich, USA.

#### 2.1.2. Instruments

All electrochemical tests were performed using an Autolab MAC80100 multichannel potentiostat/galvanostat (Metrohm, Utrecht, The Netherlands), operated with Nova 1.10.4 software.

The results obtained using the electrochemical method were confirmed using UV–Vis spectrophotometry. Spectrophotometric tests were carried out using a SPECORD 250PLUS spectrophotometer (Analytik Jena, Jena, Germany), operated with the WinAspect PLUS software version 4.2.0.0.

Scanning electron microscopy (SEM) and energy-dispersive X-ray spectroscopy (EDX) results were obtained using a Hitachi SU8230 instrument at 30 kV, 10 mA and 8 and 15 mm working distances, operated with Aztec software version 5.1 (Oxford Analytics, Oxford, UK).

Atomic force microscopy (AFM) images were obtained using a Cypher S (Asylum Research-Oxford Instruments, Santa Barbara, CA, USA) microscope. AFM measurements were performed in AC mode (tapping mode), with AC160TS-R3 silicon cantilevers (Olympus, Tokyo, Japan), with a spring constant of  $\sim 26 \text{ N/m}$  ( $8.42\text{--}57 \text{ N/m}$ ) and a resonance frequency of  $\sim 300 \pm 100 \text{ kHz}$ . Several areas of the samples were analyzed at different scan sizes (20, 10, 5 and  $2 \mu\text{m}$ ), with 256 pixels/line and with a scan rate of 1 Hz. Data acquisition and image analysis was performed using the integrated AR16 software version 16 (Asylum Research) written in the Igor Pro software package (Igor Pro 6, WaveMetrics, Inc., Lake Oswego, OR, USA). An HI208 pH-meter (Hanna Instruments, Chiba, Japan) was used to measure the pH of the prepared solutions.

## 2.2. Methods

### 2.2.1. Electrochemical Cell Printing

The electrochemical cells were printed using a previously described process [34,40], with slight modifications. A stainless steel stencil with apertures in the size and shape of the contacts and the electrodes was used for printing the cells on a plastic substrate. A rubber squeegee was used to distribute the conductive inks uniformly in the apertures. The same procedure was employed for printing all the electrochemical cell components, but different inks were used. The contacts and reference electrode were printed first using a Ag ink, followed by the working and counter electrodes, which were printed using a carbon conductive ink. Between each printing step, the electrochemical cells were dried for 15 min at 60 °C to allow for solvent evaporation and the thermal polymerization of the monomer in the ink composition. The last step consisted in the application of an insulating layer to prevent shortcuts, followed by drying overnight at 50 °C to ensure complete drying. Silver wires were attached to the end of the contacts to enable the connection of the electrodes to the potentiostat.

After printing, the electrodes were pretreated in a 1 M Na<sub>2</sub>CO<sub>3</sub> solution, using amperometry at a constant potential of +1.2 V for 600 s. This process ensured an increased sensitivity and the stabilization of the electrode signal before AuNP deposition [34].

### 2.2.2. Gold Nanoparticle Deposition

AuNPs deposition was optimized by testing different electrochemical protocols and information from previously published papers [34]. Both cyclic voltammetry (CV) and amperometry were used for AuNP deposition. In the case of CV, AuNP deposition was performed from solutions of different concentrations of HAuCl<sub>4</sub> (2.5, 5 and 10 mM) prepared in 0.5 M H<sub>2</sub>SO<sub>4</sub>, for varying numbers of cycles (20, 25 and 50). In the case of amperometry, two protocols were tested, as follows: 500 s at −0.5 V and −0.1 V (following a protocol described in the literature [41]), respectively, from a 5 mM solution of HAuCl<sub>4</sub> prepared in 0.5 M H<sub>2</sub>SO<sub>4</sub>. The optimized deposition protocol was as follows: CV from a 5 mM HAuCl<sub>4</sub> solution prepared in 0.5 M H<sub>2</sub>SO<sub>4</sub>, for 25 cycles, between −0.2 and +1.4 V, with a scan rate of 100 mV/s.

### 2.2.3. SEM, AFM and EDX Analysis

Before SEM and EDX testing, the electrodes were fixed on a carbon tape and were sprayed with a thin carbon layer. Images were captured at different magnitudes from three various points of the electrode surface. For EDX analysis, three different regions were screened from 15 mm working distance; atomic weight percent reports were generated.

AFM images were obtained using AC mode (tapping mode) in air, under normal temperature and pressure conditions, using AC160TS-R3 (Olympus) silicon cantilevers. These have an aluminum-covered reflective surface with a nominal tip radius of 7 nm, a nominal constant of 26 N/m and a resonance frequency of ~300 kHz. Multiple randomly selected surfaces were analyzed, with a resolution of 512 × 512 pixels and a scan rate between 0.5 and 1 Hz.

### 2.2.4. Electrochemical Characterization and Doxorubicin Detection

The electrochemical characterization of the electrode surface was performed after printing and after AuNP deposition, using electrochemical impedance spectroscopy (EIS) and CV in a 10 mM [Fe(CN)<sub>6</sub>]<sup>3−/4−</sup> solution prepared in 0.1 M KCl. The EIS parameters were as follows: 61 frequencies from 0.1 to 100,000 Hz; amplitude 0.01 Hz at open circuit potential (OCP). The CV parameters were as follows: scanning between −0.4 and +1 V for 2 cycles, at a scan rate of 100 mV/s.

For all DOX electrochemical experiments, DOX solution was purged with nitrogen, 10 min before testing.

The influence of the supporting electrolyte was tested using a 500 µg/mL DOX solution prepared in 0.1 M H<sub>2</sub>SO<sub>4</sub>, 0.1 M HCl, 0.1 M PBS pH 7.4 and 0.2 M carbonate buffer

pH 10, using the following DPV parameters: scan between  $-1.2$  and  $-0.4$  V, potential step 5 mV, amplitude 0.2 V, interval time 0.1 s, modulation time 0.05 s and scan rate 50 mV/s. The influence of the pH on the electrochemical detection of DOX was tested via CV on 100  $\mu\text{g}/\text{mL}$  DOX solutions prepared in Britton–Robinson buffer (BRB) with pH values between 2 and 12. The CV parameters were as follows: potential range between  $-1$  and 0 V, at a scan rate of 100 mV/s.

The influence of the scan rate on the electrochemical detection of DOX was evaluated by varying the scan rate between 5 and 500 mV/s and scanning the potential between  $-0.8$  and 0 V for 1 cycle. The tests were performed on 500  $\mu\text{g}/\text{mL}$  DOX solutions prepared in 0.1 M phosphate-buffered saline (PBS) at pH 7.4.

The influence of the DOX concentration on the analytical signal was tested via DPV using DOX solutions of different concentrations prepared in 0.1 M PBS, pH 7.4. DPV parameters were as follows: scan between  $-1.2$  and  $-0.4$  V, potential step 5 mV, amplitude 0.2 V, interval time 0.1 s, modulation time 0.05 s and scan rate 50 mV/s. A calibration curve was constructed in the domain 1–500  $\mu\text{g}/\text{mL}$  and the limit of detection (LOD) was calculated based on the  $S/N = 3$ . All electrochemical tests were performed in triplicate at 25 °C, if not stated otherwise.

Intraday stability was evaluated by performing five consecutive DPV analyses in a 100  $\mu\text{g}/\text{mL}$  DOX solution on the same electrode, with abundant washing and electrochemical cleaning in 0.5 M  $\text{H}_2\text{SO}_4$  between each test. The CV parameters for the electrochemical cleaning were as follows: potential scan between  $-0.9$  and 1.2 V for 5 cycles, with a scan rate of 100 mV/s. Interday stability was evaluated by testing a 100  $\mu\text{g}/\text{mL}$  DOX solution on five different electrodes. Stability for up to 30 days was tested weekly, using different sensors that were all printed, pretreated and functionalized with AuNPs on the same day, as well as a 100  $\mu\text{g}/\text{mL}$  DOX solution.

#### 2.2.5. Selectivity and Real Sample Analysis

The selectivity of the method was tested in the presence of common interferents that could be found in pharmaceutical formulations, such as glucose, oxalic acid, citric acid and starch (see concentrations of each interferent in Section 3.6) that were added to a 100  $\mu\text{g}/\text{mL}$  DOX solution prepared in 0.1 M PBS, pH 7.4.

Commercial human serum (Sigma-Aldrich, USA) was diluted 1:50 with 0.1 M PBS, pH 7.4 and was spiked with three different concentrations of DOX—5, 25 and 100  $\mu\text{g}/\text{mL}$ —after which the optimized DPV procedure was applied. All tests were performed in triplicate and the recoveries of the analytical signal of DOX were calculated.

#### 2.2.6. Spectrophotometric Analysis

The UV–VIS spectra of DOX solutions prepared in different buffers were traced between 250 and 650 nm to identify the  $\lambda_{\text{max}}$  of DOX. Measurements at  $\lambda_{\text{max}}$  were recorded for solutions of different concentrations of DOX to obtain calibration curves, which were used to quantify the amount of DOX released from the nanosomes in different buffers. The results obtained were compared to those obtained using the DPV method.

#### 2.2.7. DOX Loading into Nanosomes

A 2 mg/mL DOX solution was prepared in acetate buffer, pH 3 and 2 mL of the solution were put in contact with 0.1 g nanosomes for 24 h, under continuous shaking on a HulaMixer (Invitrogen, Waltham, MA, USA) under the following conditions: orbital shaking 3 r/min (60 s), reciprocal shaking 1<sup>0</sup> (10 s) and vibration movement 1<sup>0</sup> (5 s). After 24 h, the samples were centrifuged for 10 min at 12,000 r/min to separate the loaded nanosomes from the DOX-containing supernatant. In total, 250  $\mu\text{L}$  of the supernatant were diluted to 2 mL, with the appropriate volume of acetate buffer, and DPV and spectrophotometric tests were performed to determine the quantity of DOX from the supernatant and to calculate

the quantity of loaded DOX. The encapsulation efficiency (EE) and loading capacity (LC) were calculated based on the following equations [42]:

$$EE(\%) = \frac{V \times C_i - V \times C_f}{V \times C_f} \times 100 \quad (1)$$

$$LC(\%) = \frac{V \times C_i - V \times C_f}{m_{ms}} \times 100 \quad (2)$$

where  $V$ —total volume of the release media (2 mL);  $C_i$ —initial DOX concentration in the supernatant (2 mg/mL);  $C_f$ —final DOX concentration in the supernatant (after loading);  $m_{ms}$ —mass of nanosomes used for the loading process.

### 2.2.8. DOX Release

Approximately 0.1 g of loaded nanosomes was accurately weighed and placed in Eppendorf tubes, in contact with 2 mL of different release buffers, as follows: 0.1 M PBS, pH 5, 6 and 7.4. The samples were placed on a HulaMixer under the following conditions: orbital shaking 3 r/min (60 s), reciprocal shaking  $1^0$  (10 s) and vibration movement  $1^0$  (5 s) for 72 h. The samples were centrifuged for 2 min at 12,000 r/min to separate the loaded nanosomes from the DOX-containing supernatant. A total of 250  $\mu$ L of release media were sampled at precise time-points at 15 min intervals in the first hour, 1 h intervals for the following 6 h and 24 h intervals for 72 h. After each sampling, the taken volume was replaced with 250  $\mu$ L of fresh media of the appropriate pH, to maintain a constant release buffer volume of 2 mL. The samples were diluted with the appropriate buffers and DPV and UV-Vis tests were performed to determine the quantity of DOX. The cumulative release of DOX was calculated using the following equations [42]:

$$m_n = (C_n \times V) + V_s(C_1 + C_2 + C_3 + \dots + C_{n-1}) \quad (3)$$

$$C_{r_n}(\%) = \frac{m_n}{m_{load}} \times 100 \quad (4)$$

where  $m_n$ —DOX mass at a given time ( $n$ );  $C_n$ —DOX concentration in the release buffer at a given time;  $V$ —total volume of the release media;  $V_s$ —volume of release media sampled at each tested time (250  $\mu$ L);  $C_1, C_2, C_3 \dots C_n$ —concentrations of DOX in the release media at previous testing times;  $m_{load}$ —amount of DOX loaded in the nanosomes.

## 3. Results and Discussions

### 3.1. Gold Nanoparticle Deposition

AuNPs were deposited on the electrode surface using different protocols (see Section 2.2.2) and the following parameters were optimized: (1) the deposition method, (2) the  $\text{HAuCl}_4$  concentration and (3) the number of cycles, in the case of CV. To choose the optimal parameters, the electrodes were tested after AuNP deposition in the presence of a 10 mM  $[\text{Fe}(\text{CN})_6]^{3-/4-}$  solution prepared in KCl 0.1. The results are presented in Table 1, with the parameters chosen as optimal written in bold.  $I_{ox}$  represents the intensity of the oxidation current and  $E_{ox}$  represents the oxidation potential of DOX.

After AuNP deposition via CV from a 5 mM  $\text{HAuCl}_4$  solution, a significant increase in current intensity was noticed, compared to the deposition performed from a 2.5 mM solution. However, when the concentration was doubled again, to 10 mM, no significant differences were noticed, so 5 mM was chosen as the optimal concentration. Increasing the number of cycles from 20 to 25 led to an almost two-fold increase in current intensity; however, no proportional increase was noticed when the number of cycles was 50, so 25 cycles were chosen for the deposition protocol. No significant differences were observed in the CV performed in  $[\text{Fe}(\text{CN})_6]^{3-/4-}$  between the amperometric and voltammetric deposition protocols, so the CV protocol was chosen as the optimal method.

**Table 1.** Optimization of the AuNP deposition procedure.

Optimized Parameter		$I_{ox}$ ( $\mu A$ )	RSD (%)	$E_{ox}$ (V)
Deposition method	AMP at $-0.1$ V (5 mM HAuCl <sub>4</sub> )	525	8.5	0.195
	AMP at $-0.5$ V (5 mM HAuCl <sub>4</sub> )	513	1.7	0.203
	CV (5 mM HAuCl <sub>4</sub> )	541	2.8	0.220
HAuCl <sub>4</sub> concentration	2.5 mM (CV, 25 cycles)	392	3.2	0.222
	5 mM (CV, 25 cycles)	541	2.8	0.193
	10 mM (CV, 25 cycles)	563	1.9	0.189
Number of cycles	20 (5 mM HAuCl <sub>4</sub> )	456	4.3	0.210
	25 (5 mM HAuCl <sub>4</sub> )	541	2.8	0.193
	50 (5 mM HAuCl <sub>4</sub> )	584	3.7	0.188

AMP—amperometry;  $I_{ox}$ —intensity of the oxidation current;  $E_{ox}$ —oxidation potential for DOX.

### 3.2. Electrochemical Characterization of the Platform

The electrochemical behavior of the electrode surface was characterized via CV and EIS, in a 10 mM  $[Fe(CN)_6]^{3-/4-}$  solution prepared in 0.1 M KCl, at open-circuit potential after electrode printing, 1 M  $Na_2CO_3$  pretreatment and AuNP deposition (Figure 2).

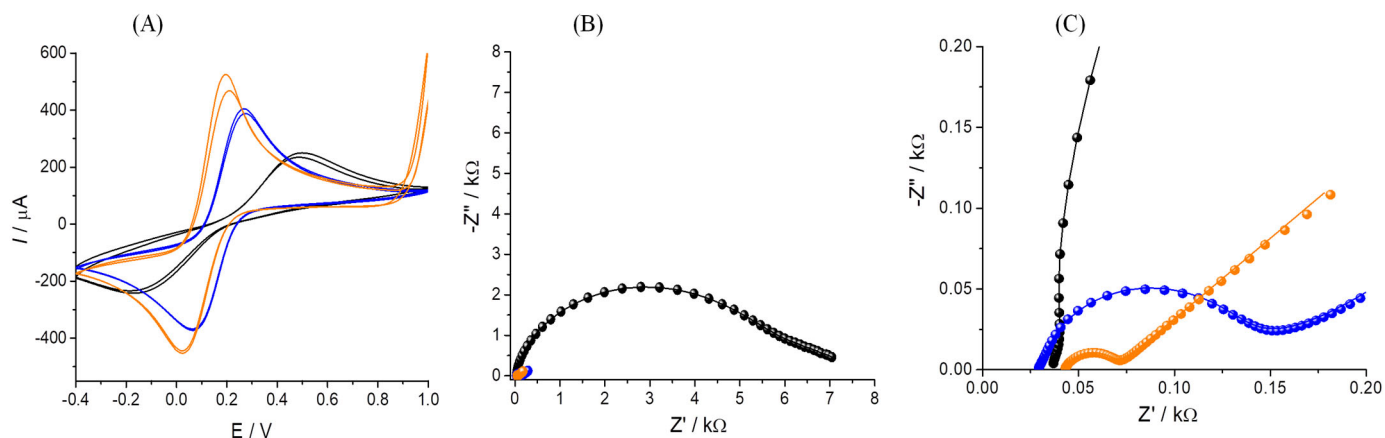


**Figure 2.** Cyclic voltammograms obtained in a 10 mM  $[Fe(CN)_6]^{3-/4-}$  solution prepared in 0.1 M KCl after different electrode fabrication steps: printing (black), 1 M  $Na_2CO_3$  pretreatment (blue) and AuNP deposition (orange) (A); Nyquist spectra obtained in a 10 mM  $[Fe(CN)_6]^{3-/4-}$  prepared in 0.1 M KCl solution after different electrode fabrication steps: printing (black), 1 M  $Na_2CO_3$  pretreatment (blue) and AuNP deposition (orange) (B); zoomed-in Nyquist spectra for the high-frequency area (C).

As can be seen in Figure 2A, after printing, the electrodes exhibited the highest peak-to-peak separation ( $\Delta E = 0.7$  V) and a low peak intensity. After the 1 M  $Na_2CO_3$  pretreatment, an increase in the peak intensity can be noticed, as well as a reduction in the peak-to-peak separation ( $\Delta E = 0.2$  V). The AuNP deposition led to the maximum peak intensity and an additional reduction in the peak-to-peak separation ( $\Delta E = 0.15$  V), indicating the electrocatalytic effect of the AuNPs.

The data obtained from CV analysis were confirmed using EIS (Figure 2B,C). The Nyquist plots obtained for the printed electrode show an  $R_{ct}$  value of 5.54 k $\Omega$ , as well as the absence of diffusion, indicating a very slow electron transfer at the electrode surface. After pretreatment and AuNP deposition, a significant decrease in the  $R_{ct}$  to 91 and 26  $\Omega$ , respectively, can be observed. A well-defined diffusion part of the Nyquist spectra was also noticed, indicating a faster electron transfer.

Based on the analyses performed at various scan rates with  $[Fe(CN)_6]^{3-/4-}$  as redox probe, the electroactive area of the pretreated, in-house printed electrodes before and after AuNP modification was calculated using the Randles–Sevcik equation (Equation (5)) and

was estimated at  $S = 0.308 \text{ cm}^2$  for the pretreated, unmodified electrode and  $S = 0.401 \text{ cm}^2$  for the AuNP modified electrode [43].

$$I_p = (2.69 \cdot 10^5) \cdot n \cdot \sqrt{\alpha \cdot n \alpha} \cdot C \cdot \sqrt{D} \cdot \sqrt{v} \cdot S \quad (5)$$

$I_p$ —current intensity;  $n$ —number of exchanged electrons;  $\alpha$ —transfer coefficient;  $C$ — $[\text{Fe}(\text{CN})_6]^{3-/4-}$  concentration ( $\text{mol}/\text{cm}^3$ );  $D$ —coefficient of diffusion ( $\text{cm}^2/\text{s}$ );  $v$ —scan rate ( $\text{V}/\text{s}$ );  $S$ —electroactive area of the working electrode ( $\text{cm}^2$ ).

By using the Nova 1.10.4 software, the EIS data were modeled using fitting and simulation options. These features facilitated the selection of equivalent circuits to articulate the mathematical framework for the individual curves. The resulting model data are detailed in Table S1.

For the unmodified electrode, the suggested equivalent circuit comprised  $[R_s(Q[R_{ct}W](R_1C_1))]$ . Here, the components encompassed the solution resistance ( $R_s$ ), inclusive of equipment and electrical circuit element resistances; charge-transfer resistance ( $R_{ct}$ ); a constant phase element (CPE) substituting the double-layer capacitance ( $C_{DL}$ ); Warburg impedance ( $W$ ) and a series of  $R$  and  $C$  in parallel ( $(R_1C_1)$ ). The choice of CPE over  $C$  was driven by deviations in real-world EIS representations, wherein distortions like depressed semicircles were more accurately characterized using CPE than  $C$ . The literature also attested to the efficacy of a circuit combining parallel CPE with a series of  $R_{ct}$  and  $W$  for porous film characterization on electrode surfaces [44]. The incorporation of the  $(R_1C_1)$  series might be attributed to the ink film's high porosity and non-uniformity post printing and drying, along with potential adsorption/desorption phenomena within the pores.

Following the electrochemical pretreatment of the electrode surface, the  $(R_1C_1)$  series in the equivalent circuit became unnecessary, possibly due to reduced surface porosity resulting from interaction with the activation solution. The  $R_{ct}$  value decreased from  $5.54 \text{ k}\Omega$  for the bare electrode to  $91 \Omega$  post-activation.

Upon electrochemical deposition of AuNPs on the electrode, the equivalent circuit used for modeling EIS data remained unchanged from the pretreatment step. This suggests that the transfer mechanism to the electrode surface remained unaltered following functionalization with highly conductive metal nanoparticles. The  $R_{ct}$  value decreased from  $91 \Omega$  post-activation to  $26 \Omega$  after AuNP functionalization. The relatively small  $\chi^2$  values (Table S1) indicated a favorable fit between experimental data and the proposed circuit and model.

### 3.3. Morphostructural Characterization of the Platform

The platform was characterized using SEM, EDX and AFM. The data obtained after SEM scanning indicated the presence of a rugged surface (Figure 3A), marked by carbon agglomerations (Figure 3B) on the bare electrode. The surface pretreatment with  $1 \text{ M Na}_2\text{CO}_3$  did not lead to significant changes in the structure of the platform. After AuNP deposition, a thin and uniform AuNP film can be observed on the surface of the electrode. The AuNPs were spherical, with a size ranging between  $80$  and  $100 \text{ nm}$  (Figure 3C,D), appearing as particles with a whiter shade than the background. SEM data indicated the successful functionalization of the carbon electrode with AuNPs.

EDX analysis was performed on the samples analyzed using SEM, indicating a relative gold composition of  $15.8 \pm 0.3\%$  after AuNP deposition (Figure 4A). The data obtained were compared to those obtained for the bare electrode (Figure 4B). Other elements detected were components of the electrode or dried material from the buffers.

AFM results confirmed the data obtained using SEM, indicating a rough surface for the bare electrode (Figure 5A,B). After AuNP deposition, it was noticed that the gold had a tendency to form a uniform layer of nanoparticles on the electrode surface (Figure 5C,D).

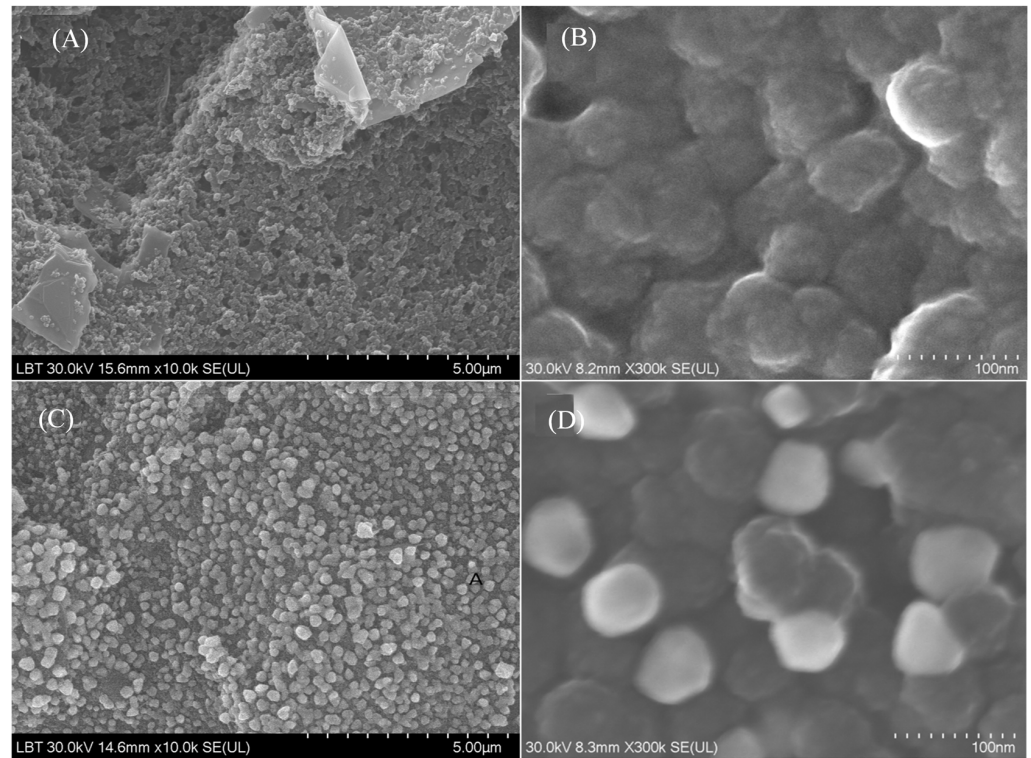


Figure 3. SEM images obtained at different magnifications before (A,B) and after AuNP deposition (C,D).

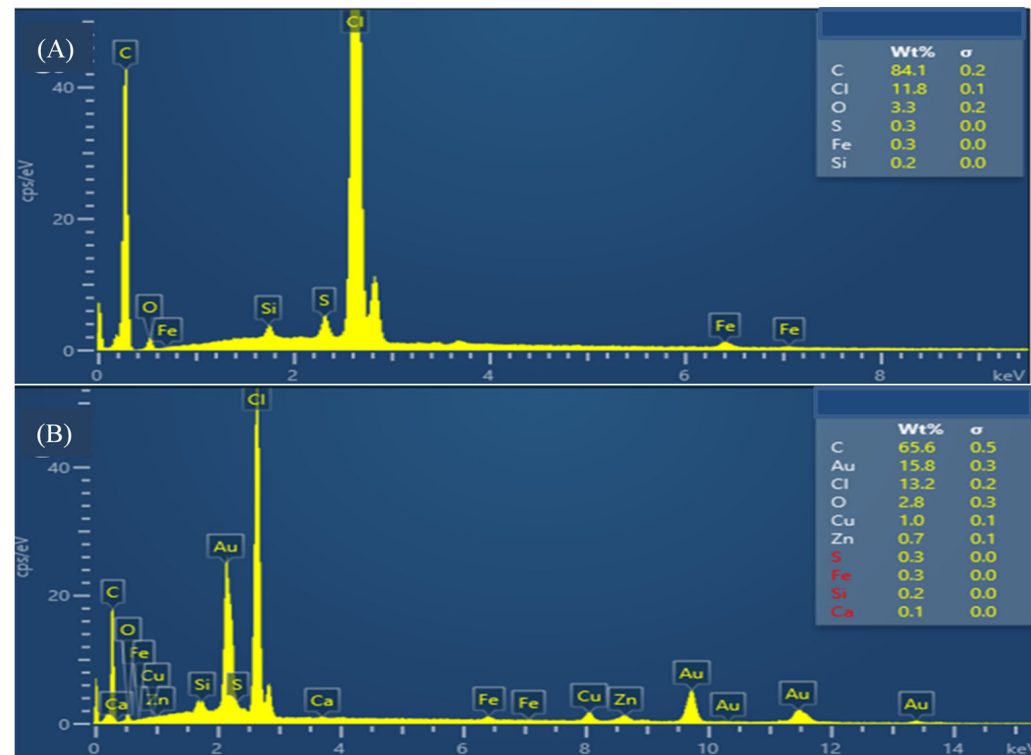
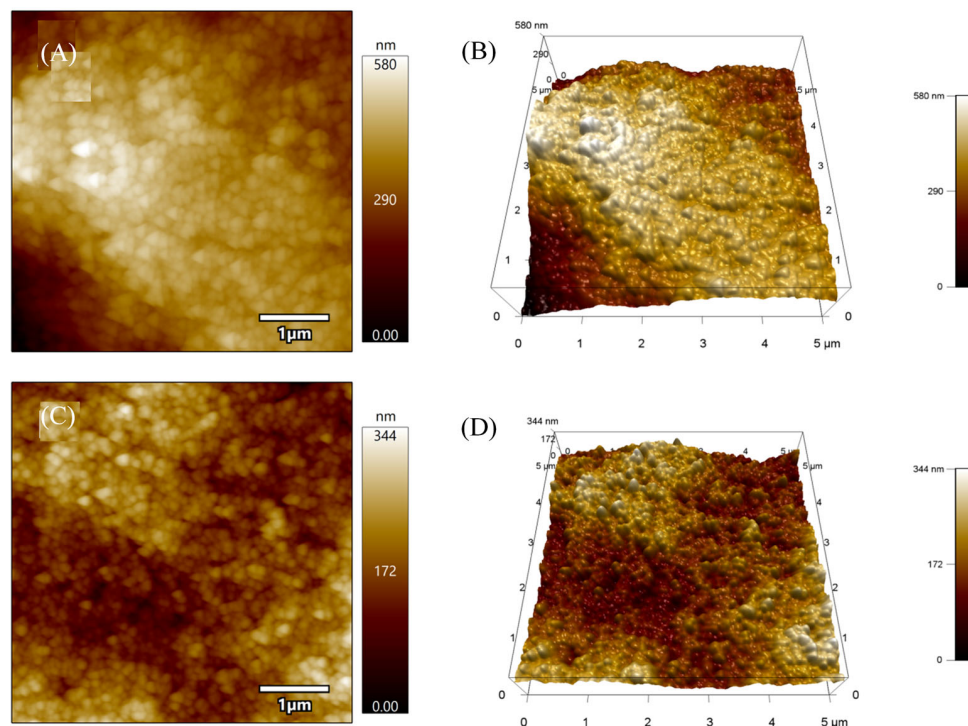


Figure 4. Elemental analysis performed using EDX for the bare printed electrode (A) and the AuNP-functionalized electrode (B).



**Figure 5.** Two-dimensional (left) and three-dimensional (right) AFM topography images before (A,B) and after AuNP deposition (C,D). Scan size—5  $\mu\text{m}$ .

### 3.4. Electrochemical Behavior of DOX

The influence of the supporting media, pH and scan rate on the electrochemical behavior of DOX were investigated using CV and DPV.

#### 3.4.1. Influence of the Supporting Electrolyte

DOX solutions were prepared in different supporting media, as follows: 0.1 M phosphate-buffered saline (PBS), pH 7.4; 0.2 M carbonate buffer, pH 10; 0.1 M HCl; 0.1 M  $\text{H}_2\text{SO}_4$ . The best results were obtained in 0.1 M  $\text{H}_2\text{SO}_4$ , where two oxidation peaks were observed for DOX, one at a potential of about 0 V, similar to data previously reported in the literature [45] (Table S2). Despite this, for the optimized detection method, PBS was used as supporting media, due to its similarity to the physiological environment and the envisaged application of the sensor, since DOX release experiments need to be performed in conditions that mimic physiological/tumor media conditions.

#### 3.4.2. Influence of the pH

To study the influence of the pH on the detection of DOX, DOX solutions were prepared in BRB with pH values between 2 and 12. The results are presented in Figure 6. The figure presents the well-defined oxidation and reduction peaks of DOX (Figures 6A and S1). These peaks appear due to the oxidation of the hydroquinone fragment to the corresponding quinone, followed by its reduction back to the hydroquinone form. This mechanism involves the transfer of two electrons and two protons, as previously reported in the literature [46] and described in the mechanism proposed in Figure 6B. It can be seen in Figure 6C that the intensity of the oxidation and reduction currents increases from pH 2 to pH 7, followed by a decrease in the alkaline pH domain, confirming the involvement of protons in the oxidation mechanism [46,47]. A cathodic shift of the oxidation/reduction peaks can also be noticed with the increase in pH (Figure 6D). This can be explained either by the involvement of protons in the electrochemical transformation mechanism or by the lower stability and solubility of DOX at higher pH values [48]. The variation of the oxidation and reduction potential with the pH were represented graphically and were linear on the pH domain 2–9 (Table 2).

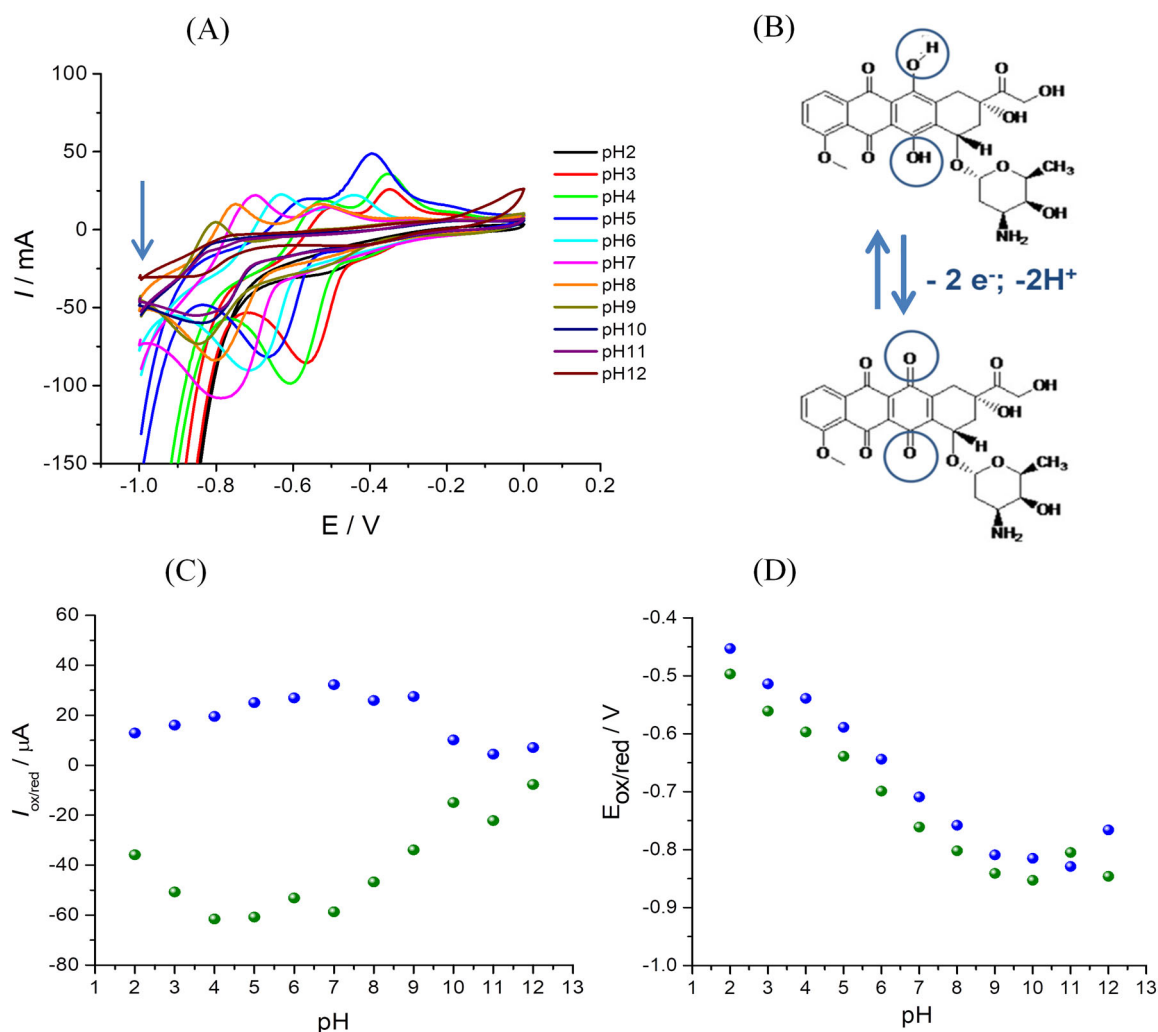


**Figure 6.** Cyclic voltammograms obtained for 100  $\mu\text{g}/\text{mL}$  DOX solutions prepared in BRB, pH 2–12; The arrow indicates the starting potential in the voltammograms; (A); mechanism proposed for the oxidation of DOX (B); variation of the oxidation (blue) and reduction (green) peaks with the pH (C) and variation of the oxidation (blue) and reduction (green) potentials with the pH (D).

**Table 2.** The variation of the DOX oxidation and reduction potentials with the pH.

$E_{\text{ox}} = f(\text{pH})$	Oxidation	$E_{\text{Ox}} = -0.051 \text{ pH} - 0.347$	$R^2 = 0.994$
$E_{\text{red}} = f(\text{pH})$	Reduction	$E_{\text{Red}} = -0.050 \text{ pH} - 0.402$	$R^2 = 0.996$

### 3.4.3. Influence of the Scan Rate

The influence of the scan rate was tested on 500  $\mu\text{g}/\text{mL}$  DOX solutions prepared in 0.1 M PBS, pH 7.4, using scan rates between 5 and 500 mV/s. The results are presented in Figure 7. It can be noticed that the increase in scan rate leads to an anodic shift of the oxidation potentials and a cathodic shift of the reduction potentials (Figure 7A). This variation suggests that the electrochemical process is controlled by adsorption, which is further confirmed by the variation of the current intensity with the scan rate (Figure 7C), which presents a better linear correlation compared to the variation of the current intensity with the square root of the scan rate (Figure 7D). The data in Figure 7C,D were obtained using scan rates between 5 and 400 mV/s. In Figure 7D, two different linearity regions can be observed, while, for the variation of  $I$  with the scan rate, the correlation coefficients indicate linearity on the whole domain. This confirms the observations in Figure 7A. Moreover, the  $\log I$  vs.  $\log v$  representation (Figure 7B) presents a good linearity, a correlation coefficient of  $R^2 = 0.994$  and a slope of 0.9, which is close to the theoretical value of 1

that is specific for adsorption-controlled processes, further proving that the process is adsorption-controlled [47,49].

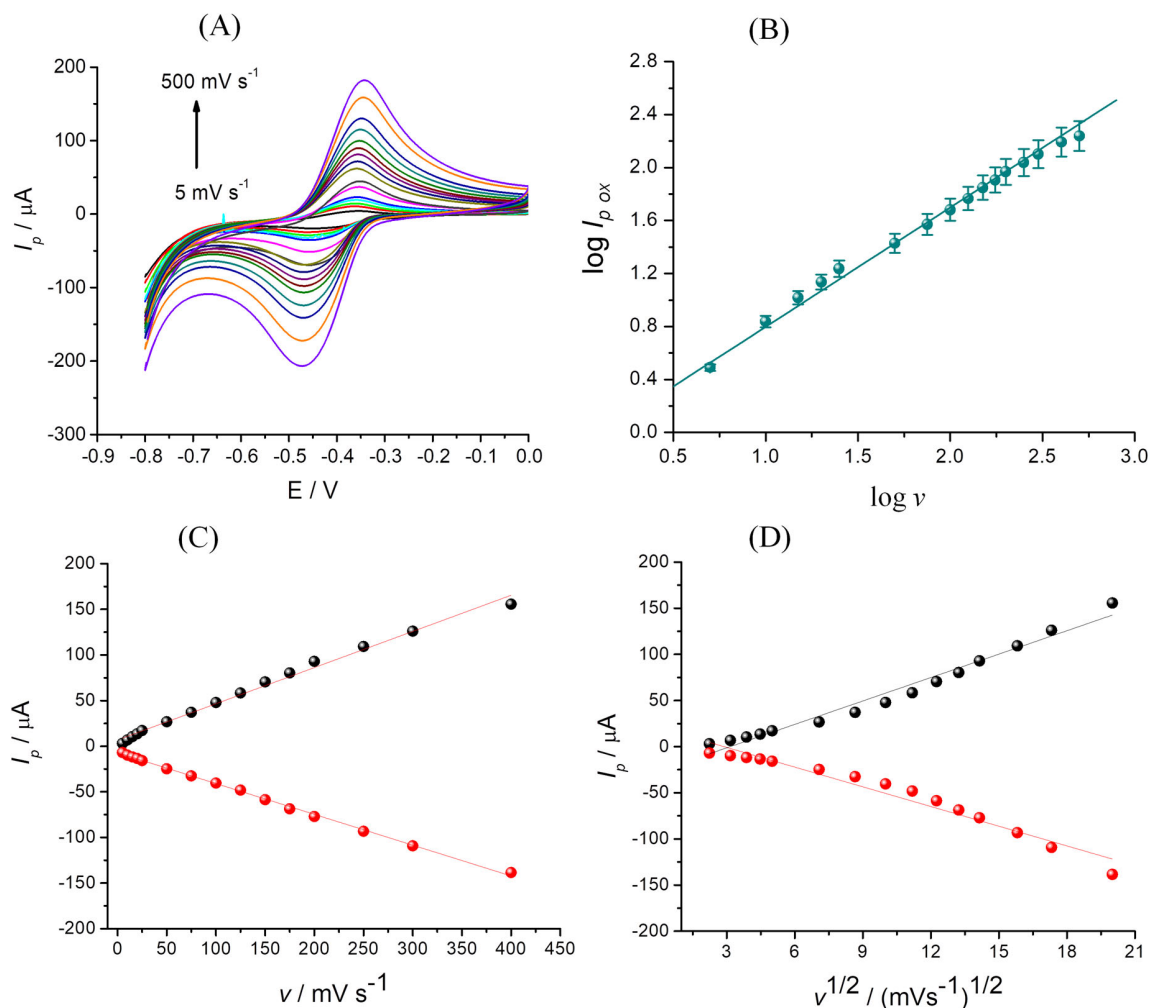


**Figure 7.** Cyclic voltammograms obtained for 500  $\mu\text{g}/\text{mL}$  DOX solutions prepared in 0.1 M PBS, pH 7.4, at different scan rates (A); variation of the logarithm of the oxidation current with the logarithm of the scan rate (B); variation of the current peak with the scan rate (C) and square root of the scan rate (D).

The equations, together with the  $R^2$  values for each variation, are represented in Table 3. The scan rate that was chosen for further experiments was 50 mV/s.

**Table 3.** Parameters and equations that characterize the variation of the current intensity with the scan rate, the current intensity with the square root of the scan rate and the logarithm of the current intensity with the logarithm of the scan rate.

$I = f(v)$	Oxidation	$I_{\text{Ox}} = 0.39 v + 6.87$	$R^2 = 0.996$
	Reduction	$I_{\text{Red}} = -0.33 v - 7.15$	$R^2 = 0.998$
$I = f(v^{1/2})$	Oxidation	$I_{\text{Ox}} = 8.46 v^{1/2} - 26.61$	$R^2 = 0.973$
	Reduction	$I_{\text{Red}} = -7.11 v^{1/2} + 20.50$	$R^2 = 0.954$
$\log I_{\text{Ox}} = f(\log v)$	Oxidation	$\log I_{\text{Ox}} = 0.90 \log v - 0.10$	$R^2 = 0.994$

### 3.5. Electrochemical Detection of DOX

A DPV method was used for the detection of DOX from solutions prepared in 0.1 M PBS, pH 7.4 (Figure 8A). Increasing concentrations of DOX were used to obtain the dependence

between the concentration and the analytical signal; the data were represented to construct the calibration curve (Figure 8B,C). The correlation between the two parameters was logarithmic, characterized using the equation:  $I_{ox} (\mu A) = 26.45 \log(\text{DOX concentration} / \mu\text{g mL}^{-1}) - 19.13$ ;  $R^2 = 0.976$ . A dynamic range between 1 and 500  $\mu\text{g/mL}$  was obtained and an LOD of 0.3  $\mu\text{g/mL}$  was estimated. The LOD was calculated based on the standard deviation of ten blank measurements, multiplied by three and divided by the slope of the calibration curve. The estimated RSD for the whole tested domain was 4.26%. The LOQ was equal to the lowest concentration in the dynamic range, 1  $\mu\text{g/mL}$ , and the sensitivity was  $7.82 \mu\text{A mL } \mu\text{g}^{-1}$ . The obtained parameters were compared to previously published data (Table 4).

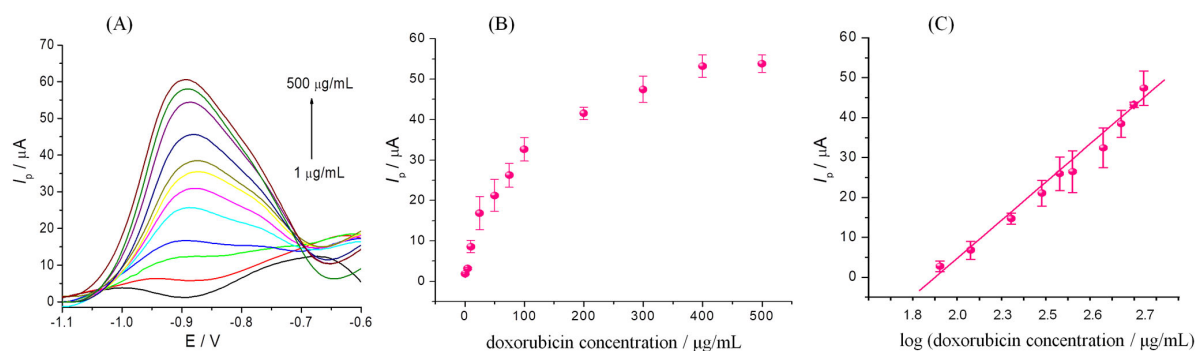


**Figure 8.** Differential pulse voltammograms obtained for increasing concentrations of DOX, as follows: 1; 5; 10; 25; 50; 75; 100; 200; 300; 400; 500  $\mu\text{g/mL}$ , prepared in 0.1 M PBS, pH 7.4. DPV parameters—scan between  $-1.2$  and  $-0.4$  V, potential step 5 mV, amplitude 0.2 V, interval time 0.1 s, modulation time 0.05 s and scan rate 50 mV/s. Blank test (0.1 M PBS, pH 7.4) represented with black line (A); variation of the current intensity with the DOX concentration (B) and logarithmic calibration curve (C). Error bars represent the standard deviation for three measurements.

**Table 4.** Comparison of the developed method with data presented in the literature.

Electrode Used	Detection Method	Linear Range ( $\mu\text{M}$ )	LOD (nM)	Matrix	Ref.
GCE/AgNP/Chi	SWV	0.103–8.6	103 (LOQ)	Human plasma Cell lysate	[35]
PtE/MWCNT	CV	0.09–7.33	3.6	Human plasma	[36]
GCE/Au@AuPt/3D ZnO-GO	DPV	0.65–369.45	13	Urine	[38]
p-AgSAE	DPCSV	0.6–10	440	Tap water, urine	[39]
PLLI	DPV	1–40	840	Buffers	
GCE/N-CNOs	DPV	0.0002–10	0.06	Serum	[45]
GCE/GQDs	DPV	0.018–3.600	16	Human plasma	[46]
CPE/SDS	CV	10–80	1120	Buffer	[47]
SPE	DPV	2–24	390		
SPE	AMP	0.91–119	180	Pharmaceutical formulations	[48]
GCE/CD-GN	DPV	0.01–0.2	0.1	Buffer	[49]
GCE/AB	CV	0.01–2.5 $\mu\text{M}$	3.006 nM	Spiked human serum	[50]
CPE/GO/MOF	DPV	0.01–100	5	Injectable solution	[51]
PGE	LSV	10–60	9900	Serum	[52]
<b>SPE/AuNP</b>	<b>DPV</b>	<b>1.83–915 <math>\mu\text{M}</math></b>	<b>550</b>	<b>Pharmaceutical formulations Spiked serum</b>	<b>This work</b>

PtE—platinum electrode; MWCNT—multi-walled carbon nanotubes; GCE—glassy carbon electrode; AB—acetylene black; GQDs—graphene quantum dots; CPE—carbon paste electrode; GO—graphene oxide; MOF—metal organic framework; AgNP—silver nanoparticles; Chi—chitosan; PGE—pencil graphite electrode; SPE—screen-printed electrode; AuNP—gold nanoparticles; CV—cyclic voltammetry; DPV—differential pulse voltammetry; SWV—square wave voltammetry; LSV—linear scan voltammetry; p-AgSAE—polished silver amalgam electrode; DPCSV—differential pulse cathodic stripping voltammetry; PLLI—polarized liquid–liquid interface; N-CNOs—nitrogen-doped carbon nanooxions; SDS—sodium dodecyl sulfate; AMP—amperometry; CD-GN—cyclodextrin–graphene hybrid nanosheets.

Despite the higher LOD of the developed method, the present work aims primarily to detect DOX in pharmaceutical formulations, thereby providing a sufficiently low LOD for its intended purpose. Complex electrode functionalization [45] can substantially decrease the LOD; however, the method becomes more cumbersome, while not providing additional benefits for DOX detection from pharmaceutical formulations. Moreover, the present method has a wide linear range and was successfully applied on spiked biological fluids. Direct detection of DOX represents a quick and facile method compared to other strategies, such as detection using the interaction of DNA with DOX, which, although sensitive, can pose stability concerns [36]. Additionally, the detection can be performed quickly and in a cost-efficient manner, with an estimated cost of EUR 1/fabricated electrode. The in-house printed electrodes are designed for single-use applications, thus avoiding the possibility of surface fouling from one test to another, as well as avoiding the surface cleaning and polishing required in the case of platinum and glassy-carbon electrodes. Moreover, screen-printed electrodes present the advantage of miniaturization, opening new perspectives for the detection of DOX using portable potentiostats.

### 3.6. Stability, Selectivity and Real Sample Analysis

Intra-electrode stability was tested at least five times on the same electrode, using a 100 µg/mL DOX solution with abundant washing and a 0.5 M H<sub>2</sub>SO<sub>4</sub> electrochemical pretreatment between tests, due to the adsorptive nature of the electrochemical process. The recovery of the analyte obtained for these tests was very good and an RSD value of 5.81% was obtained. The RSD value obtained from tests on five different electrodes for inter-electrode stability was 4.15%. Stability, for up to 30 days, was tested weekly, reaching 92% (±4.36%) after 30 days.

The selectivity of the sensor was evaluated in the presence of common interferents found in pharmaceutical formulations or serum, such as glucose, oxalic acid, citric acid and starch. Neither of the tested substances presented significant interferences with the DOX detection, as can be seen in Table 5.

**Table 5.** Selectivity and real sample analysis parameters and recoveries.

Sample	Recovery (%)	RSD (%)	
100 µg/mL DOX +10 µg/mL oxalic acid	111.71	1.11	
100 µg/mL DOX + 10 µg/mL citric acid	98.57	3.46	
100 µg/mL DOX + 10 µg/mL starch	81.19	2.04	
100 µg/mL DOX + 1000 µg/mL glucose	99.46	1.97	
Tests in human serum 1:50			
DOX concentration (µg/mL)		Recovery (%)	RSD (%)
Added	Found		
5	5.47	109.42	3.67
25	24.38	97.52	2.59
100	113.21	113.21	1.46

The monitoring of DOX serum concentrations can help to ensure therapeutic efficiency and reduce adverse reactions. DOX serum concentration monitoring is also important for comparing treatment methods and evaluating the efficiency of different pharmaceutical formulations based on their DOX release profiles in serum [53]. All this justifies the application of the developed sensor on serum samples. Different DOX concentrations were spiked into commercial serum samples, but the recoveries obtained were too low, so the serum was diluted with 0.1 M PBS, pH 7.4, in a ratio of 1:50. Good recoveries, ranging from 97.52% to 113.21% (calculated as average of three measurements for each sample), were obtained with RSD values between 1.46% and 3.67%, after minimal sample pretreatment (dilution with buffer) (Table 5).

### 3.7. DOX Spectrophotometric Behavior

A spectrophotometric method for DOX quantification was used as a control. DOX solutions of different concentrations were prepared in all used solvents and the maximum absorption of DOX was registered in all cases. The calibration curves obtained for all solutions are presented in Table S3.

### 3.8. DOX Loading

The loading of nanosomes was performed from a 2 mg/mL DOX solution prepared in acetate buffer, pH 3, due to the lower solubility of DOX at higher pH values. The solution was left in contact with the nanosomes for 24 h, followed by centrifugation.

The spectra obtained for DOX before and after incubation with the nanosomes indicate a decrease in the absorbance, corresponding to a decrease in the DOX concentration in the solution, indicating the successful loading of DOX in the nanosomes (Figure S2). While spectrometry can be applied to monitor the drug loading process, there are many advantages to using an electrochemical method, similar to the one proposed in this work. First, the sample volumes required for DPV are much smaller compared to spectrometry. Thus, the method is more economical and eco-friendly. Moreover, in the initial stages of pharmaceutical formulation development, small batches of pharmaceutical formulations are developed, so the number of samples is generally limited. Secondly, while method optimization can be difficult, once optimized, a DPV method can be used with minimum training, even by non-specialized personnel. Moreover, DPV methods can be applied in a decentralized and portable manner.

The EE and LC were calculated using both the UV–Vis and the optimized DPV method and the results obtained (Table 6) were similar, indicating the applicability of the electrochemical method for the characterization of the loading process.

**Table 6.** Comparison of the loading parameters calculated using the UV–Vis and DPV methods.

Loading Solution	Quantification Method	EE (%)	LC (%)
2 mg/mL DOX in acetate buffer pH 3	UV–Vis	41.15	1.48
	DPV	42.95	1.54

### 3.9. DOX Release

The release of DOX from the loaded nanosomes was evaluated in 0.1 M PBS, pH 5, 6 and 7.4, and the cumulative release was determined using the DPV (Figure 9A) and UV–Vis methods (Figure 9B). The release was the most efficient at pH 6, followed by pH 5 and pH 7.4. Images of the nanosome suspensions after different steps of the loading and release processes are presented in Figure S2.

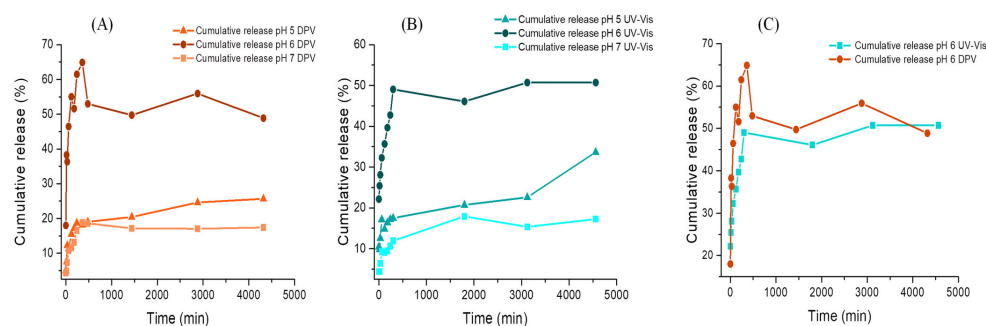


**Figure 9.** Cumulative release of DOX from the nanosomes detected using the DPV (A) and spectrophotometric (B) methods. (C) Cumulative release profiles obtained for DOX at pH 6 using the optimized DPV (brown) and UV–Vis methods (blue). DPV parameters—scan between  $-1.2$  and  $-0.4$  V, potential step 5 mV, amplitude 0.2 V, interval time 0.1 s, modulation time 0.05 s and scan rate 50 mV/s. UV–Vis parameters—absorbance measurement at  $\lambda_{\max} = 482$  nm.

A higher release at pH 6 is convenient for drug delivery applications, since it is known that the pH of tumor tissues is more acidic than that of healthy tissues [54,55]. The cumulative release profiles obtained at pH 6 with the DPV and UV–Vis methods were compared (Figure 9C) and an average correlation of 94.32% (RSD 7.74) was determined, considering a 72 h release time.

The relatively low difference between the two methods can be attributed to differences in the sensitivity of the procedures, the DPV showing a superior sensitivity. The good correlation between the results indicates the applicability of the DPV method for the control of the release of DOX from nanosomes.

#### 4. Conclusions

In conclusion, this study successfully developed an electrochemical sensor for the detection of DOX, using in-house screen-printed electrodes modified with AuNPs to enhance sensitivity. The reversible oxidation of DOX at the electrodes occurred through an adsorption-based process. The optimized DOX detection method was based on DPV and exhibited a wide dynamic range between 1 and 500  $\mu\text{g/mL}$ , as well as a low detection limit. The sensor's efficacy was further demonstrated through its application in the quality control of novel DOX-loaded nanosomes, providing a quantification of DOX loading and release. Comparative analysis with UV–Vis spectrophotometry yielded consistent results, affirming the reliability of the electrochemical method. This study represents a significant advancement in pharmaceutical formulation control, with high potential for the optimized electrochemical method application for formulation stages.

This opens new perspectives in the field of pharmaceutical formulation control, demonstrating that electrochemical methods could be successfully used in the formulation stage due to their numerous advantages such as portability, rapidity and accuracy.

**Supplementary Materials:** The following supporting information can be downloaded at: <https://www.mdpi.com/article/10.3390/chemosensors12040069/s1>, Figure S1: UV–Vis spectra of the DOX loading solution before (black) and after incubation with the nanosomes (red); Figure S2. Images of the nanosome suspensions before (A1) and after (A2) loading from a 2 mg/mL DOX solution prepared in acetate buffer. Images of the nanosome suspensions after 72 h of release in PBS, pH 5 (B1) and pH 7.4 (B2). Table S1. Values of the EIS parameters derived from the equivalent circuit through the fitting and simulation option of the software at each step of the sensor elaboration protocol. Table S2. Influence of the supporting electrolyte on the detection of DOX from a 500  $\mu\text{g/mL}$  solution. Table S3. Calibration curves obtained for DOX in PBS of different pH values.

**Author Contributions:** Conceptualization, A.P., M.T. and C.C.; Data curation, D.B. and M.S.; Methodology, A.P., M.T., I.B., D.B. and M.S.; Formal analysis, A.P., M.T., I.B., D.B. and M.S.; Investigation, A.P., M.T. and I.B.; Writing—original draft, A.P., M.T., I.B. and S.M. Writing—review and editing, M.T., S.M. and C.C.; Project administration, M.T. and C.C.; Resources, M.T. and C.C.; Supervision, S.M. and C.C. All authors have read and agreed to the published version of the manuscript.

**Funding:** This work was supported by the Romanian Ministry of Education and Research, CNCS-UEFISCDI, project number PN–III–P1–1.1–TE–2021–1543. DB acknowledges financial support from the MCID through the Nucleu Program within the National Plan for Research, Development, and Innovation 2022–2027, project PN 23 24 01 05.

**Institutional Review Board Statement:** Not applicable.

**Informed Consent Statement:** Not applicable.

**Data Availability Statement:** Dataset available on request from the authors.

**Acknowledgments:** A.P. acknowledges UMF internal PCD grant no. 649/5/11.01.2024.

**Conflicts of Interest:** The authors declare no conflicts of interest.

## References

1. Sritharan, S.; Sivalingam, N. A comprehensive review on time-tested anticancer drug doxorubicin. *Life Sci.* **2021**, *278*, 119527. [CrossRef]
2. Johnson-Arbor, K.; Dubey, R. Doxorubicin. Stat Pearls. Available online: <https://www.ncbi.nlm.nih.gov/books/NBK459232/#article-20695.s11> (accessed on 5 December 2023).
3. Luu, A.Z.; Chowdhury, B.; Al-Omran, M.; Teoh, H.; Hess, D.A.; Verma, S. Role of Endothelium in Doxorubicin-Induced Cardiomyopathy. *JACC Basic Transl. Sci.* **2018**, *3*, 861–870. [CrossRef]
4. Kalyanaraman, B. Teaching the basics of the mechanism of doxorubicin-induced cardiotoxicity: Have we been barking up the wrong tree? *Redox Biol.* **2020**, *29*, 101394. [CrossRef]
5. Mirhadi, E.; Mashreghi, M.; Askarizadeh, A.; Mehrabian, A.; Alavizadeh, S.H.; Arabi, L.; Badiie, A.; Jaafari, M.R. Redox-sensitive doxorubicin liposome: A formulation approach for targeted tumor therapy. *Sci. Rep.* **2022**, *12*, 11310. [CrossRef]
6. Iman, M.; Moosavian, S.A.; Zamani, P.; Jaafari, M.R. Preparation of AS1411 aptamer-modified PEGylated liposomal doxorubicin and evaluation of its anti-cancer effects in vitro and in vivo. *J. Drug Deliv. Sci. Technol.* **2023**, *81*, 104255. [CrossRef]
7. Shahraki, N.; Mehrabian, A.; Amiri-Darban, S.; Moosavian, S.A.; Jaafari, M.R. Preparation and characterization of PEGylated liposomal Doxorubicin targeted with leptin-derived peptide and evaluation of their anti-tumor effects, in vitro and in vivo in mice bearing C26 colon carcinoma. *Colloids Surf. B Biointerfaces* **2021**, *200*, 111589. [CrossRef]
8. Sonju, J.J.; Shrestha, P.; Dahal, A.; Gu, X.; Johnson, W.D.; Zhang, D.; Muthumula, C.M.R.; Meyer, S.A.; Mattheolabakis, G.; Jois, S.D. Lyophilized liposomal formulation of a peptidomimetic-Dox conjugate for HER2 positive breast and lung cancer. *Int. J. Pharm.* **2023**, *639*, 122950. [CrossRef]
9. Chen, H.; Sun, R.; Zheng, J.; Kawazoe, N.; Yang, Y.; Chen, G. Doxorubicin-encapsulated thermosensitive liposome-functionalized photothermal composite scaffolds for synergistic photothermal therapy and chemotherapy. *J. Mater. Chem. B* **2022**, *10*, 4771–4782. [CrossRef]
10. Bahrami Parsa, M.; Tafvizi, F.; Chaleshi, V.; Ebadi, M. Preparation, characterization, and Co-delivery of cisplatin and doxorubicin-loaded liposomes to enhance anticancer Activities. *Heliyon* **2023**, *9*, e20657. [CrossRef]
11. Aloss, K.; Hamar, P. Recent Preclinical and Clinical Progress in Liposomal Doxorubicin. *Pharmaceutics* **2023**, *15*, 893. [CrossRef]
12. O'Brien, M.E.R.; Wigler, N.; Inbar, M.; Rosso, R.; Grischke, E.; Santoro, A.; Catane, R.; Kieback, D.G.; Tomczak, P.; Ackland, S.P.; et al. Reduced cardiotoxicity and comparable efficacy in a phase III trial of pegylated liposomal doxorubicin HCl (CAELYX/Doxil) versus conventional doxorubicin for first-line treatment of metastatic breast cancer. *Ann. Oncol. Off. J. Eur. Soc. Med. Oncol.* **2004**, *15*, 440–449. [CrossRef]
13. Saharkhiz, S.; Zarepour, A.; Nasri, N.; Cordani, M.; Zarrabi, A. A comparison study between doxorubicin and curcumin co-administration and co-loading in a smart niosomal formulation for MCF-7 breast cancer therapy. *Eur. J. Pharm. Sci.* **2023**, *191*, 106600. [CrossRef]
14. Saharkhiz, S.; Zarepour, A.; Zarrabi, A. A new theranostic pH-responsive niosome formulation for doxorubicin delivery and bio-imaging against breast cancer. *Int. J. Pharm.* **2023**, *637*, 122845. [CrossRef] [PubMed]
15. Bofill-Bonet, C.; Gil-Vives, M.; Artigues, M.; Hernández, M.; Borrós, S.; Fornaguera, C. Fine-tuning formulation and biological interaction of doxorubicin-loaded polymeric nanoparticles via electrolyte concentration modulation. *J. Mol. Liq.* **2023**, *390*, 122986. [CrossRef]
16. Cé, R.; Couto, G.K.; Pacheco, B.Z.; Dallemole, D.R.; Paschoal, J.D.; Pacheco, B.S.; Guterres, S.S.; Seixas, F.; Collares, T.; Pohlmann, A.R. Folic acid-doxorubicin polymeric nanocapsules: A promising formulation for the treatment of triple-negative breast cancer. *Eur. J. Pharm. Sci.* **2021**, *165*, 105943. [CrossRef]
17. Jindal, D.; Sinha, S.; Agarwal, V.; Sisodia, V.; Singh, M. Combinatorial Assessment of Doxorubicin with Chlorogenic acid by in silico studies and development of its polymeric-nanoparticle against breast cancer. *Mater. Today Proc.* **2023**. [CrossRef]
18. Akram, M.U.; Abbas, N.; Farman, M.; Manzoor, S.; Khan, M.I.; Osman, S.M.; Luque, R.; Shanableh, A. Tumor micro-environment sensitive release of doxorubicin through chitosan based polymeric nanoparticles: An in-vitro study. *Chemosphere* **2023**, *313*, 137332. [CrossRef]
19. Gökşen Tosun, N.; Erden Tayhan, S.; Gökçe, İ.; Alkan, C. Doxorubicin-loaded mPEG-pPAD-mPEG triblock polymeric nanoparticles for drug delivery systems: Preparation and in vitro evaluation. *J. Mol. Struct.* **2023**, *1291*, 135959. [CrossRef]
20. Kunene, S.C.; Lin, K.-S.; Weng, M.-T.; Carrera Espinoza, M.J.; Lin, Y.-S.; Wu, C.-M.; Tsai, W.-C. Dual stimuli-responsive polymeric microgels for enhanced doxorubicin delivery to hepatocellular carcinoma. *J. Drug Deliv. Sci. Technol.* **2023**, *87*, 104776. [CrossRef]
21. Sheikh, A.; Abourehab, M.A.S.; Tulbah, A.S.; Kesharwani, P. Aptamer-grafted, cell membrane-coated dendrimer loaded with doxorubicin as a targeted nanosystem against epithelial cellular adhesion molecule (EpCAM) for triple negative breast cancer therapy. *J. Drug Deliv. Sci. Technol.* **2023**, *86*, 104745. [CrossRef]
22. Hashemi, H.; Namazi, H. Understanding the pH dependent fluorescence and doxorubicin release from graphene oxide functionalized citric acid dendrimer as a highly efficient drug delivery system. *Mater. Today Commun.* **2021**, *28*, 102593. [CrossRef]
23. Michlewska, S.; Garaiova, Z.; Šubjakova, V.; Hołota, M.; Kubczak, M.; Grodzicka, M.; Okła, E.; Naziris, N.; Balcerzak, Ł.; Ortega, P.; et al. Lipid-coated ruthenium dendrimer conjugated with doxorubicin in anti-cancer drug delivery: Introducing protocols. *Colloids Surf. B Biointerfaces* **2023**, *227*, 113371. [CrossRef]

24. Carrera Espinoza, M.J.; Lin, K.S.; Weng, M.T.; Kunene, S.C.; Lin, Y.S.; Liu, S.Y. Magnetic boron nitride nanosheets-based on pH-responsive smart nanocarriers for the delivery of doxorubicin for liver cancer treatment. *Colloids Surf. B Biointerfaces* **2023**, *222*, 113129. [[CrossRef](#)] [[PubMed](#)]
25. Zhao, Q.; Xie, P.; Li, X.; Wang, Y.; Zhang, Y.; Wang, S. Magnetic mesoporous silica nanoparticles mediated redox and pH dual-responsive target drug delivery for combined magnetothermal therapy and chemotherapy. *Colloids Surf. A Physicochem. Eng. Asp.* **2022**, *648*, 129359. [[CrossRef](#)]
26. Wang, J.; Zhu, F.; Li, K.; Xu, J.; Li, P.; Fan, Y. pH-responsive mesoporous Fe<sub>2</sub>O<sub>3</sub>-Au nanomedicine delivery system with magnetic targeting for cancer therapy. *Med. Nov. Technol. Devices* **2022**, *15*, 100127. [[CrossRef](#)]
27. Liu, Q.; Tan, Z.; Zheng, D.; Qiu, X. pH-responsive magnetic Fe<sub>3</sub>O<sub>4</sub>/carboxymethyl chitosan/aminated lignosulfonate nanoparticles with uniform size for targeted drug loading. *Int. J. Biol. Macromol.* **2022**, *225*, 1182–1192. [[CrossRef](#)] [[PubMed](#)]
28. Maliszewska, O.; Plenis, A.; Olędzka, I.; Kowalski, P.; Miękus, N.; Bień, E.; Krawczyk, M.A.; Adamkiewicz-Drożynska, E.; Bączek, T. Optimization of LC method for the quantification of doxorubicin in plasma and urine samples in view of pharmacokinetic, biomedical and drug monitoring therapy studies. *J. Pharm. Biomed. Anal.* **2018**, *158*, 376–385. [[CrossRef](#)] [[PubMed](#)]
29. Yamamoto, E.; Miyazaki, S.; Aoyama, C.; Kato, M. A simple and rapid measurement method of encapsulation efficiency of doxorubicin loaded liposomes by direct injection of the liposomal suspension to liquid chromatography. *Int. J. Pharm.* **2018**, *536*, 21–28. [[CrossRef](#)]
30. Harahap, Y.; Suryadi, H.; Anarta, A. Development and Validation of Doxorubicin Hydrochloride and Doxorubicinol Quantification Method in Dried Blood Spot by Liquid Chromatography-Tandem Mass Spectrometry. *J. Pharm. Bioallied Sci.* **2020**, *12*, 406–412. [[CrossRef](#)]
31. Saklani, R.; Tiwari, A.K.; Yadav, P.K.; Yadav, P.; Chourasia, M.K. Validated HPLC-UV Method for Simultaneous Estimation of Paclitaxel and Doxorubicin Employing Ion Pair Chromatography: Application in Formulation Development and Pharmacokinetic Studies. *Biomed. Res. Int.* **2022**, *2022*, 7708235. [[CrossRef](#)]
32. Ji, Y.; Zhang, X.; Liu, J.; Chen, Y.; Meng, M.; Li, C.; Wang, L. Direct quantitation of free, encapsulated, total doxorubicin and doxorubicinol in stabilized frozen human plasma to support a BE study of liposomal doxorubicin. *J. Pharm. Biomed. Anal.* **2020**, *189*, 113388. [[CrossRef](#)]
33. Han, J.; Zhang, J.; Zhao, H.; Li, Y.; Chen, Z. Simultaneous determination of doxorubicin and its dipeptide prodrug in mice plasma by HPLC with fluorescence detection. *J. Pharm. Anal.* **2016**, *6*, 199–202. [[CrossRef](#)] [[PubMed](#)]
34. Tertis, M.; Zăgrean, M.; Pusta, A.; Suci, M.; Bogdan, D.; Cristea, C. Innovative nanostructured aptasensor for the electrochemical detection of gluten in food samples. *Microchem. J.* **2023**, *193*, 109069. [[CrossRef](#)]
35. Ehsani, M.; Soleymani, J.; Mohammadalizadeh, P.; Hasanzadeh, M.; Jouyban, A.; Khoubnasabjafari, M.; Vaez-Gharamaleki, Y. Low potential detection of doxorubicin using a sensitive electrochemical sensor based on glassy carbon electrode modified with silver nanoparticles-supported poly(chitosan): A new platform in pharmaceutical analysis. *Microchem. J.* **2021**, *165*, 106101. [[CrossRef](#)]
36. Hajian, R.; Tayebi, Z.; Shams, N. Fabrication of an electrochemical sensor for determination of doxorubicin in human plasma and its interaction with DNA. *J. Pharm. Anal.* **2017**, *7*, 27–33. [[CrossRef](#)] [[PubMed](#)]
37. Ganesh, P.-S.; Govindasamy, M.; Kim, S.-Y.; Choi, D.-S.; Ko, H.-U.; Alshgari, R.A.; Huang, C.-H. Synergetic effects of Mo<sub>2</sub>C sphere/SCN nanocatalysts interface for nanomolar detection of uric acid and folic acid in presence of interferences. *Ecotoxicol. Environ. Saf.* **2023**, *253*, 114694. [[CrossRef](#)] [[PubMed](#)]
38. Shi, L.; Wang, Z.; Bai, L.; Yang, G. Preparation of 3D Nanoflower-like ZnO/graphene Oxide decorated with Au@AuPt Bimetallic Nanoparticles for Electrochemical Determination of Doxorubicin Hydrochloride. *Int. J. Electrochem. Sci.* **2022**, *17*, 220144. [[CrossRef](#)]
39. Skalová, Š.; Langmaier, J.; Barek, J.; Vyskočil, V.; Navrátil, T. Doxorubicin determination using two novel voltammetric approaches: A comparative study. *Electrochim. Acta* **2020**, *330*, 135180. [[CrossRef](#)]
40. Ciui, B.; Tertis, M.; Feurdean, C.N.; Ilea, A.; Sandulescu, R.; Wang, J.; Cristea, C. Cavitas electrochemical sensor toward detection of N-epsilon (carboxymethyl)lysine in oral cavity. *Sens. Actuators B Chem.* **2019**, *281*, 399–407. [[CrossRef](#)]
41. Shao, Y.; Dong, Y.; Bin, L.; Fan, L.; Wang, L.; Yuan, X.; Li, D.; Liu, X.; Zhao, S. Application of gold nanoparticles/polyaniline-multi-walled carbon nanotubes modified screen-printed carbon electrode for electrochemical sensing of zinc, lead, and copper. *Microchem. J.* **2021**, *170*, 106726. [[CrossRef](#)]
42. Rus, I.; Tertis, M.; Cristea, C.; Sandulescu, R. Modern Analytical Techniques for Drug Delivery Systems Characterization. *Curr. Anal. Chem.* **2020**, *16*, 1–10. [[CrossRef](#)]
43. Elgrishi, N.; Rountree, K.J.; McCarthy, B.D.; Rountree, E.S.; Eisenhart, T.T.; Dempsey, J.L. A Practical Beginner's Guide to Cyclic Voltammetry. *J. Chem. Educ.* **2018**, *95*, 197–206. [[CrossRef](#)]
44. Tertis, M.; Leva, P.I.; Bogdan, D.; Suci, M.; Graur, F.; Cristea, C. Impedimetric aptasensor for the label-free and selective detection of Interleukin-6 for colorectal cancer screening. *Biosens. Bioelectron.* **2019**, *137*, 123–132. [[CrossRef](#)] [[PubMed](#)]
45. Ghanbari, M.H.; Norouzi, Z. A new nanostructure consisting of nitrogen-doped carbon nanoions for an electrochemical sensor to the determination of doxorubicin. *Microchem. J.* **2020**, *157*, 105098. [[CrossRef](#)]
46. Hashemzadeh, N.; Hasanzadeh, M.; Shadjou, N.; Eivazi-Ziaei, J.; Khoubnasabjafari, M.; Jouyban, A. Graphene quantum dot modified glassy carbon electrode for the determination of doxorubicin hydrochloride in human plasma. *J. Pharm. Anal.* **2016**, *6*, 235–241. [[CrossRef](#)] [[PubMed](#)]

47. Deepa, S.; Swamy, B.E.K.; Pai, K.V. A surfactant SDS modified carbon paste electrode as an enhanced and effective electrochemical sensor for the determination of doxorubicin and dacarbazine its applications: A voltammetric study. *J. Electroanal. Chem.* **2020**, *879*, 114748. [[CrossRef](#)]
48. Rus, I.; Tertiş, M.; Barbălată, C.; Porfire, A.; Tomuță, I.; Săndulescu, R.; Cristea, C. An Electrochemical Strategy for the Simultaneous Detection of Doxorubicin and Simvastatin for Their Potential Use in the Treatment of Cancer. *Biosensors* **2021**, *11*, 15. [[CrossRef](#)] [[PubMed](#)]
49. Guo, Y.; Chen, Y.; Zhao, Q.; Shuang, S.; Dong, C. Electrochemical Sensor for Ultrasensitive Determination of Doxorubicin and Methotrexate Based on Cyclodextrin-Graphene Hybrid Nanosheets. *Electroanalysis* **2011**, *23*, 2400–2407. [[CrossRef](#)]
50. Sun, S.; Xu, X.; Niu, A.; Sun, Z.; Zhai, Y.; Li, S.; Xuan, C.; Zhou, Y.; Yang, X.; Zhou, T.; et al. Novel Electrochemical Sensor Based on Acetylene Black for the Determination of Doxorubicin in Serum Samples. *Int. J. Electrochem. Sci.* **2022**, *17*, 221187. [[CrossRef](#)]
51. Shamsadin-Azad, Z.; Ali Taher, M.; Beitollahi, H. Metal organic framework-235/graphene oxide nanocomposite modified electrode as an electrochemical sensor for the voltammetric determination of doxorubicin in presence of dacarbazine. *Microchem. J.* **2024**, *196*, 109580. [[CrossRef](#)]
52. Deepa, S.; Kumara Swamy, B.E.; Vasantakumar Pai, K. Voltammetric detection of anticancer drug Doxorubicin at pencil graphite electrode: A voltammetric study. *Sensors Int.* **2020**, *1*, 100033. [[CrossRef](#)]
53. Harahap, Y.; Ardiningsih, P.; Corintias Winarti, A.; Purwanto, D.J. Analysis of the Doxorubicin and Doxorubicinol in the Plasma of Breast Cancer Patients for Monitoring the Toxicity of Doxorubicin. *Drug Des. Devel. Ther.* **2020**, *14*, 3469–3475. [[CrossRef](#)] [[PubMed](#)]
54. Thews, O.; Riemann, A. Tumor pH and metastasis: A malignant process beyond hypoxia. *Cancer Metastasis Rev.* **2019**, *38*, 113–129. [[CrossRef](#)] [[PubMed](#)]
55. Attia, M.F.; Anton, N.; Wallyn, J.; Omran, Z.; Vandamme, T.F. An overview of active and passive targeting strategies to improve the nanocarriers efficiency to tumour sites. *J. Pharm. Pharmacol.* **2019**, *71*, 1185–1198. [[CrossRef](#)]

**Disclaimer/Publisher’s Note:** The statements, opinions and data contained in all publications are solely those of the individual author(s) and contributor(s) and not of MDPI and/or the editor(s). MDPI and/or the editor(s) disclaim responsibility for any injury to people or property resulting from any ideas, methods, instructions or products referred to in the content.